Evolution of Thermoelectric Properties in the Triple Cation Zintl Phase: $Yb_{13-x}Ca_xBaMgSb_{11}$ (x = 1 – 6)

Christopher J. Perez,[1] Giacomo Cerretti,[2] Elizabeth L. K. Wille,[1] Kasey P. Devlin,[1] Navtej S. Grewal,[1] Andrew P. Justl,[1] Maxwell Wood,[2] Sabah K. Bux,[2] and Susan M. Kauzlarich[1*]

[1] Department of Chemistry, University of California, One Shields Avenue, Davis, CA 95616, USA.

[2] Thermal Energy Conversion Research and Advancement Group, Jet Propulsion Laboratory, California Institute of Technology, 4800 Oak Grove Drive, Pasadena, CA 91109-8099, USA.

* Corresponding author: smkauzlarich@ucdavis.edu

Abstract:

The band structure of $Yb_{14}MgSb_{11}$ is tuned by substituting the more earth abundant cations, Ca and Ba, on the four crystallographically distinct Yb sites ($Yb_{13-x}Ca_xBaMgSb_{11}$ (x = 1, 2, 3, 4, 5, 6)). Single crystals of composition $Yb_{9.7(2)}Ca_{3.85(5)}Ba_{0.29(4)}Mg_{1.13(3)}Sb_{11.0(1)}$ were grown from Sn flux revealing the cation site preferences. Magnetic measurements on this crystal show paramagnetic behavior consistent with the presence of ~0.85 Yb^{3+}. High purity samples (> 98 %) with compositions close to nominal of $Yb_{13-x}Ca_xBaMgSb_{11}$ (x = 1– 6) were prepared by ball milling and spark plasma sintering. The carrier concentration can be rationalized with the presence of Yb^{3+} for all samples and decreases as a function of x in a systematic fashion at room temperature and increases above ~ 600 K for x = 3 – 6. The temperature dependence of the carrier concentration can be understood considering the electronic structure with a light and heavy band valence band contributing to the properties and suggests the involvement of a localized flat band or impurity state that is active with increasing amounts of Ca. The effect of temperature leads to sustained high Seebeck coefficients with low electrical resistivity arising from the transitioning of the light to heavy band with localization of carriers in the flat band or impurity state for Ca rich compositions. Speed of sound measurements showing that the lattice stiffens with increasing x. Despite the stiffening lattice, thermal conductivity decreases until x = 3, 4 at which point it increases slightly. The x = 4 sample reaches a peak figure of merit (zT)

of 1.32 at 1273 K while being 16% lighter by molar mass compared to $Yb_{14}MnSb_{11}$ thereby providing a more power dense material.

1 Introduction.

Thermoelectric materials are the heart of thermoelectric generators, solid state direct heat to electricity devices that function through the Seebeck effect.[1] The Seebeck effect takes place when a temperature gradient causes diffusion of charge carriers from hot to cold thereby generating current. Thermoelectric performance is defined by zT which is a dimensionless parameter derived from the Carnot efficiency and is dependent on the material's electrical resistivity (ρ), Seebeck coefficient (α), and total thermal conductivity (κ_{tot}) as shown in eq. 1.[2, 3]

$$zT = \frac{S^2 T}{\rho \kappa_{tot}} \quad (1)$$

These three properties are entangled by carrier concentration (n_H) and carrier mobility (μ) making zT difficult to optimize. Fortunately, κ_{tot} (eq. 2) has a lattice component ($\kappa_{lattice} = \kappa_l$) that is only dependent on crystal and microstructure.

$$(\kappa_{total} = \kappa_{electronic} + \kappa_l) \quad (2)$$

Substituting multiple atoms of different atomic masses on the same atomic sites has been known to cause scattering of high energy phonons, which are not typically scattered by phonon-phonon interactions, leading to decreased κ_l. This phenomenon known as alloy scattering has been supported experimentally in triply substituted Skutterudites ($Ba_uLa_vYb_wCo_4Sb_{12}$) which show a reduction in κ_l due to large frequency ranges of lattice phonons tuned by the substitutions.[4] $(Eu_{0.5}Yb_{0.5})_{1-x}Ca_xMg_2Bi_2$ (1-2-2) is another material with triple ion substitution that induce a 30% increase in zT by largely reducing κ_l.[5]

Zintl phases, due to complex structures that lead to low thermal conductivities and easy chemical substitutions, have in large part been a focus of thermoelectric research in the last couple of decades.[6] In particular, compounds of the $A_{14}MPn_{11}$ (14-1-11) composition, where A sites can accommodate rare earth and alkali earth metals; M site can be occupied by group 13 metals, Mn, Zn, Mg, and Pn site can be the heavier group 15 elements

(pnictogens, P-Bi), have gained fame as some of the most stable and best performing *p*-type thermoelectric materials at high temperatures.[7] Of the 14-1-11 family of compounds $Yb_{14}MnSb_{11}$ and $Yb_{14}MgSb_{11}$ stand out with peak *zT*'s of 1.35 and 1.26 respectively.[8, 9] While these materials have adequate electronic properties, the large *zT* is mostly due to the outstandingly low thermal conductivity due to the size and complexity of the unit cell shown in Figure 1. The structure and extensive substitution possibilities were recently described.[7] In brief, the structure crystallizes in the tetragonal space group $I4_1/acd$ and has four unique cation A sites with Pn coordination of about six. The Pn atoms accept electrons supplied by the cations to form isolated Pn^{3-} anions, three atom linear Pn_3^{7-} anions, and with the M elements to form MPn_4^{9-} tetrahedra, all with the goal of satisfying valence.[6] The structure has four crystallographic A sites where substitutions of differently sized elements demonstrate site preferences.[10-14]

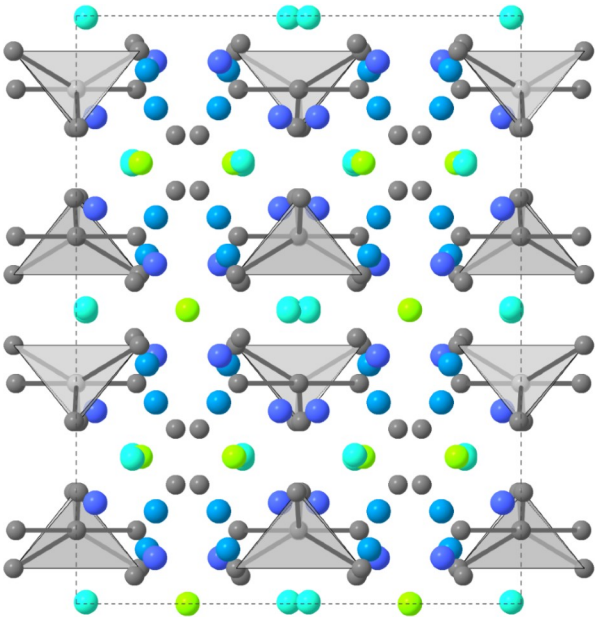

Figure 1: A view of the $A_{14}MPn_{11}$ (A = alkaline earth, rare earth metals; M = group 13 metals, Mn, Zn, Mg; Pn = P-Bi group 15 elements) unit cell along the *a/b* axis. Cation sites are color coded according to crystallographic site, A1 in purple, A2 in teal, A3 in green, and A4 in blue. The MPn_4 tetrahedra are light grey polyhedra, and the Pn anions are shown in dark grey.

One of the issues associated with the metallurgic solid-state synthesis of $Yb_{14}MSb_{11}$ (M = Mn, Mg) is the dispersion of the M element which is 1/26 atoms within the reactive

Yb/M/Sb mixture leading to M deficient phases such as $Yb_{11}Sb_{10}$ which is metallic and can have the effect of reducing Seebeck and increasing thermal conductivity leading to a lower *zT*. Grebenkemper, et al.[8] resolved this issue by employing MnSb as a means to deliver clean Mn that was easier to disperse. This resulted in *zT*'s for $Yb_{14}MnSb_{11}$ as high as 1.35 with $Yb_{11}Sb_{10}$ concentrations as low as 10 mass % after thermal cycling as determined by powder X-ray diffraction (PXRD). Justl, et al.[9] used MgH_2 to synthesize a $Yb_{14}MgSb_{11}$ sample with less than 5% mass $Yb_{11}Sb_{10}$ leading to a peak *zT* of 1.26. From a device perspective, the average *zT* (ZT_{avg}) integrated over the whole operating temperature range is more important than peak *zT*,[15] and high purity $Yb_{14}MgSb_{11}$ provided a similar ZT_{avg} compared to $Yb_{14}MnSb_{11}$ (1.10 vs 1.07).[9]

The fact that $Yb_{14}MgSb_{11}$ has a ZT_{avg} of similar value to $Yb_{14}MnSb_{11}$ provided incentive for further optimization of $Yb_{14}MgSb_{11}$ to increase the thermoelectric efficiency. At the highest temperatures the *zT* of $Yb_{14}MgSb_{11}$, which has a lower carrier concentration than $Yb_{14}MnSb_{11}$ due to the presence of ~$0.85Yb^{3+}$, decreases because of minority carrier activation known as bipolar conduction leading to increased thermal conductivity and reduced Seebeck coefficients.[9, 16] The mitigation of bipolar conduction in *p*-type PbTe-12% doped with K has in part been attributed to band gap expansion and carrier concentration increase, both of which enhance the energy barrier for promotion of minority carriers into the conduction band.[17, 18] Experimentally $Ca_{14}MgSb_{11}$[19] and $Ba_{14}MnSb_{11}$[20] have large, semiconducting resistivities that decrease as a function of temperature indicating the compounds have a larger bandgap than $Yb_{14}MgSb_{11}$. Additionally, peak thermoelectric performance in $Yb_{14}MSb_{11}$ (M = Mn, Mg) is seen above 1200 K where the unit cell is expanded by up to 1.6% (98 $Å^3$ in $Yb_{14}MgSb_{11}$).[19, 21] Therefore, starting with a larger unit cell by substituting Ba and Ca for Yb should lead to a higher *zT* at a lower temperatures by changing the components of the valence band.

We have recently shown that the band structures of $Yb_{14}MSb_{11}$ (M = Mn, Mg, Al) and $Ca_{14}MgSb_{11}$ consist of a light band at the Γ point (VB_1) and a heavy band (VB_2) with high valley degeneracy (N_v = 8) between N and P on the Fermi surface.[22] This three band model, VB_1, VB_2 and a conduction band (CB_1), successfully explains the temperature dependence of the thermal conductivity, along with other transport properties for the solid solution,

$Yb_{14}Mg_{1-x}Al_xSb_{11}$. The reported band structures for $Ca_{14}MgSb_{11}$,[19] $A_{14}MgSb_{11}$ (A = Sr, Eu),[23] and $A_{14}MgBi_{11}$ (A = Ca, Sr, Eu)[24] have similar features initially highlighted in $A_{14}MnBi_{11}$ (A = Ca, Sr, Ba) and $Ca_{14}GaAs_{11}$.[25, 26] The main difference in band structures between the A = Yb, Ca analogs of $A_{14}MgSb_{11}$ is that the band gap is larger for the Ca analog, consistent with experimental data for $Ca_{14}MgSb_{11}$.[19, 22] Incorporating Ca into $Yb_{14}MgSb_{11}$ has an additional advantage for radioisotope thermoelectric generators (RTGs) for space application as it leads to a 30% reduction in weight by molar mass (for $x = 6$) leading to a more power dense device.

In this study, single crystals of $Yb_{13-x}Ca_xBaMgSb_{11}$ ($x \sim 4$) were prepared by Sn flux to provide information on the site preferences of the cations and the magnetic properties have been measured to determine the presence of Yb^{3+}. Bulk samples of $Yb_{13-x}Ca_xBaMgSb_{11}$ (x = 1, 2, 3, 4, 5, 6) were prepared from ball-milling the elements with MgH_2, densifying *via* spark plasma sintering, and characterized up to high temperature (1273 K) to study the evolution of thermoelectric properties as the unit cell becomes progressively larger with selective cation substitution. Lattice thermal conductivity, κ_l, is expected to decrease due to alloy scattering, and bipolar conduction mitigated upon widening of the bandgap with cation substitution. The reported band structures of $Yb_{14}MgSb_{11}$ and $Ca_{14}MgSb_{11}$ are employed to rationalize the evolution of transport properties.[19, 23]

2 Experimental.

2.1 Materials. All materials were handled in an Ar glove box with < 0.1 PPM of O_2. Yb filings ~3 x ½ x ½ mm (Edge Tech, 99.999%) were obtained by brushing a Yb ingot to remove oxide and produced using a steel rasp. Larger Yb pieces (~200 mg, cut from the same ingot) were used for single crystal growth. Dendritic Ca (Sigma Aldrich, 99.99%) brushed and cut to ~20 mg pieces, Ba rod (Sigma Aldrich, 99.9%) brushed and cut into ~20 mg pieces, MgH_2 (Alfa Aesar, 98%), Sb shot (99.999%, 5Nplus), and Sn granules (Mallinckrodt, 99.97%) were used.

2.2 Single crystal growth. Synthesis of single crystals was performed using Sn flux as described in the literature.[27-30] In brief, Yb, Ca, Ba, Mg, Sb and Sn were placed, in that order, into a Canfield crucible set[31] in the ratio 10 Yb: 2.5 Ca: 2 Ba: 6 Mg: 11 Sb: 100 Sn.

The crucible was then jacketed in quartz under partial vacuum (1/5 atm Ar) and placed in a box furnace. The sample was heated standing to 873 K at 200 K/hr, let dwell for 1 hr to allow materials to outgas, then heated to 1223 K at 200 K/hr. The sample was held at temperature for 1 hr, then cooled to 1023 K at 1.6 K/hr. Once at 1023 K the sample was inverted and centrifuged hot to remove the Sn flux. The stoichiometric ratio had excess Ba and Mg to overcome the loss of the elements to vaporization.

2.3 Electron microprobe analysis (EMPA). Pellets and single crystals of $Yb_{13-x}Ca_xBaMgSb_{11}$ were mounted in epoxy and metallographically ground to a 0.1 μm finish using an oil-based diamond suspension then carbon coated for analysis. Elemental analysis was done using a JEOL JXA-8200 electron probe microanalyzer equipped with five wavelength dispersive X-ray spectrometers. $YbPO_4$, anorthite, benitoite, MgO, and Sb were used as the Yb, Ca, Ba, Mg, and Sb standards, respectively. The stoichiometry of the samples was calculated from eight atomic percent values which were averaged and multiplied by 26 to give the stoichiometry and is provided in Supporting Information (SI), Table S1.

2.4 Single crystal X-ray diffraction. Single crystals were mounted onto a polymer loop for diffraction experiments. Data were acquired on a Bruker Duo CCD diffractometer using Mo Kα radiation (λ = 0.71073 Å) under nitrogen stream (90 K) and collected with the Bruker APEX III software. Data reduction was done with SAINT and absorption correction was performed using SADABS.[32, 33] The structure solution was performed with SHELXS/SHELXL 2016/6.[34] The structure solution initially started with all cation sites filled by Yb. Ba has an ionic radii similar to La, which has been shown to preferentially occupy the Yb(2) and Yb(4) sites,[12] so was added to those sites and refined, employing the SUMP command to restrain the total occupancy of the sites to be fully occupied. Ca was added to all four sites and the occupancies refined. Because the EMPA of the single crystal showed a slight excess of Mg, similar to previously published results,[29] Mg was initially added to the Yb(1) and Yb(3) sites and the occupancies refined. The amount of Mg on the Yb(3) site refined to zero, so it was removed from that site. The final model had reasonable displacement parameters and provided a composition consistent with the EMPA results with good refinement statistics. The atomic coordinates and equivalent isotropic displacement parameters, anisotropic displacement parameters, and selected bond distances and angles are provided in SI (Tables S2-S4).

2.5 Magnetic measurements. Magnetic susceptibility data were acquired using a Quantum Design Magnetic Property Measurement System from 300 K to 2 K with an applied field of 5 T. A single crystal of 1.8 mg was sandwiched between two straws for measurement.

2.6 Metallurgical synthesis. Synthesis was adapted from literature.[8, 9, 16, 35] Yb, Ca, Ba, MgH_2, Sb, and two 10.7 g tungsten carbide balls were placed in a 55 mL tungsten carbide vial purchased from SPEX sample prep which was hermetically sealed using custom Viton O-rings. Reaction batches were a total of 9 g and the nominal stoichiometry $Yb_{13-x}Ca_xBaMg_{1.2}Sb_{11}$ was employed. The 0.2 molar excess of MgH_2 was used to overcome the high dispersity required for the low stoichiometric element, Mg. The elements and MgH_2 were milled in a SPEX 8000M mixer mill for 30 minutes. The vial was then flipped and milled an additional 30 minutes, then scraped clean using a chisel and the powder is reinserted for another 30 minutes of milling. The resulting black powder is split in half then sealed in two 10 mm Nb tube under Ar which are jacketed under vacuum with a quartz tube. The sealed tube is then heated to 1273 K at 50 K/hr, held at temperature for 96 hr and cooled to room temperature at 50 K/hr. The resulting smooth black powder is sieved through a 100 mesh screen with special care to remove any stray Nb pieces that arise from Nb tube embrittlement by the hydrogen gas in preparation for spark plasma sintering.

2.7 Spark Plasma Sintering (SPS). Powder consolidation was done with a Dr. Sinter Jr 211LX-SPS under dynamic vacuum. ~3 g of powder was packed into a 12.7 mm diameter graphite die sealed with graphite foils and graphite plungers. The die was placed into the SPS and initially 3 kN of force was applied. The sample was heated to 873 K over 5 min, heated to 898 K over 1 min, and dwelled at 898 K for 2 min during which the pressure was increased to 6 kN. The sample was then heated to 1198 K over 3 min and held at temperature for 15 min before cooling to room temperature in ~20 min. The resulting metallic/grey cylinders were sectioned and polished for thermoelectric and mechanical property measurements.

2.8 Powder X-ray diffraction (PXRD). Data were collected at room temperature using a Bruker D8 Eco Advanced at 40 kV and 25 mA from 10° – 90° 2θ at a 0.019° interval. Rietveld refinement was performed with the Jana2006 software package using structural models CIF of $Yb_{10.15}Ca_{3.42}Ba_{0.25}Mg_{1.18}Sb_{11}$ provided herein and Yb_2O_3 CIF from literature.[36, 37] The

background was fit and a sample height correction was performed. A pseudo-Voigt function was used to generate the profile. Rietveld refinement plots are provided in Figure S1 and results are tabulated in Table S4, SI.

2.9 Resistivity and Hall effect measurements. Resistivity and Hall effect measurements were conducted simultaneously under high vacuum in a home built apparatus using the Van der Pauw method, tungsten pressure contacts, and a 0.8 T field.[38] Data were fit with a sixth order polynomial for zT calculation. Experimental data are provided in SI, Figure S2.

12.10 Scanning Electron Microscopy (SEM). SEM was performed with a Scios Dual beam SEM/FIB. An Everheart-Thornley Detector was used to obtain secondary electron images. Samples were embedded in epoxy and metallographically polished to a 1 μm finish then carbon coated for imaging.

2.11 Seebeck. The Seebeck coefficient was measured on a homebuilt apparatus using the Light-pulse method.[39] Data were fit with a sixth order polynomial for zT calculation. Experimental data are shown in Figure S2.

2.12 Speed of Sound: Speed of sound measurements were performed on sintered pellets using the pulse eco method at room temperature with an Olympus 38DL plus with a V156-RM shear wave transducer and a M202-RM longitudinal wave transducer. V_L and V_T were calculated according to eq. (3). Poisson's ratio was calculated with eq. (4). The Young's and shear modulus were calculated with eq. (5) and (6) where d is defined as density measured by the Archimedes method.

$$V_{T\ or\ L} = \frac{Thickness}{Round\ trip\ transit\ time/2} \quad (3), \quad Poisson's\ Ratio\ (\nu) = \frac{1 - 2\left(\frac{V_T}{V_L}\right)^2}{2 - 2\left(\frac{V_T}{V_L}\right)^2} \quad (4),$$

$$Young's\ Modulus = \frac{{V_L}^2 d(1+\nu)(1-2\nu)}{1-\nu} \quad (5), \quad Shear\ Modulus = {V_T}^2 d \quad (6).$$

2.13 Thermal Conductivity. Thermal diffusivity was measured on flat and parallel pellets coated with graphite spray using a Netzsch Laser Flash Analysis 457 from 300 to 1273 K. Thermal conductivity was calculated using eq. (7) where d is the room temperature density described in section 2.12 scaled by coefficient of thermal expansion as described in literature[8] and expanded upon in section 2.15, D is measured diffusivity

which is plotted in SI, Figure S2, and C_P is the experimental heat capacity of $Yb_{14}MnSb_{11}$ adjusted by molar mass (eq. (8)). Eq. (9) and eq.(10) were used to calculate κ_l where ρ is resistivity and α is the Seebeck coefficient at a given temperature.[3]

$$\kappa_{tot} = d\ x\ D\ x\ C_P \quad (7), \quad C_P = \frac{C_P(Yb_{14}MnSb_{11})\ M.M(Yb_{14}MnSb_{11})}{M.M.(A_{14}MPn_{11})} \quad (8),$$

$$\kappa_l = \kappa_{tot} - \kappa_e,\ \kappa_e = LT\frac{1}{\rho} \quad (9),$$

$$L = 1.5 + e^{\frac{|\alpha|}{116}}\ x\ 10^{-8}\ \frac{W}{K^2\Omega} \quad (10).$$

2.14 Thermal Conductance. Room temperature thermal conductance (and Seebeck) were measured on a custom-made device using the comparative thermal conductance measurement method.[40] The disk-shaped sample is placed between two thermocouples (that allow a precise control of the temperature of the top and bottom faces of the sample) and then between two sets of Pyroceram reference samples, before being closed in between the hot (top) and cold (bottom) side copper blocks where another set of thermocouples measure the temperature and the voltage. This stack is spring loaded and each surface is coated with a conductive paste to ensure a uniform contact between layers and avoid air gaps. The chamber where the setup is located is then closed and kept under vacuum for the whole time of the measurement. A temperature gradient of about 25 degrees is applied between the hot and cold side of the stack. Using the reading of the thermocouples placed on the top and bottom surfaces of the sample, the developed program calculated the thermal conductance and the Seebeck. Single point thermal conductance measurements of $Yb_7Ca_6BaMgSb_{11}$ yield a thermal conductivity value of 0.27(3) J/gK at 300 K which is consistent with the adjusted heat capacity employed for the $x = 6$ sample.

2.15 Dilatometry and Coefficient of Thermal Expansion (CTE). The coefficient of thermal expansion was measured under flowing Argon using a Netzsch Dil 402 C dilatometer in the temperature range 300-1273 K. A rod-shaped sample, about 9 mm long, was inserted into an alumina sample holder and brought into contact with the pushrod. Upon heating (and cooling), the thermal expansion of the sample is detected by a displacement system connected to the pushrod. Knowing the initial length (L_0) of the sample, the measured temperature gradient (ΔT) and the change in length (ΔL), the coefficient of thermal expansion can be derived with the following equation:

$$CTE = \frac{1}{L_0}\frac{\Delta L}{\Delta T} \quad (11)$$

Results are summarized in Figure S3. CTE was measured for the $Yb_7Ca_6BaMgSb_{11}$ compound (x = 6) and found to be 18 PPM/K which is close to that of $Yb_{14}MnSb_{11}$ (16.0 PPM/K) previously measured.[21] A linear relationship between Ca content (*x* fraction) and CTE was assumed and used to calculate CTE for each composition.

3 Results and discussion.

3.1 Single Crystal Structure. Single crystals were grown from Sn flux to investigate the structural properties of this quinary phase. Table 1 contains information about the structure solution and Tables S2, S3 (SI) contains fractional positional coordinates for the atoms isotropic and anisotropic thermal parameters. EMPA of the single crystal employed for data collection gave the formula $Yb_{9.7(2)}Ca_{3.85(5)}Ba_{0.29(4)}Mg_{1.13(3)}Sb_{11.0(1)}$, close to that obtained from the refinement of the single crystal data: $Yb_{10.15}Ca_{3.42}Ba_{0.25}Mg_{1.18}Sb_{11}$. Structural solution employed EMPA stoichiometries as a starting point for the occupancies of the octahedral Yb sites (see Figure 2). There are four crystallographically unique A sites in the structure type and for $Yb_{14}MgSb_{11}$ designated as Yb(1)-Yb(4). Detailed analysis of these four sites for $Yb_{14}MnSb_{11}$ is described by atomic Hirshfeld surface analysis.[41] The concept applied to atoms in a crystal defines the volume and the sphericity providing Yb(1) and Yb(3) with the smallest volumes and Yb(2) and Yb(4) with the largest volumes, with sphericity about the same for all.[41] As mentioned in the Introduction, site preferences of cation substitutions to date chiefly correlate with size.[10-14] Although this is the first example of the $A_{14}MSb_{11}$ structure prepared with three cations, the site preferences correlation appears to be consistent with the relative cation sizes. The excess Mg (0.13(3) excess) is also noted in literature[29] where Mg^{2+} is seen to occupy not only the tetrahedral site, but also partially occupies the smaller, less distorted Yb1 and Yb3 sites; therefore, Mg was initially refined on the Yb1 and Yb3 sites and was determined to occupy the Yb1 site. Larger cations, such as La are known to preferentially occupy the larger more distorted Yb2 and Yb4 sites.[12] This is observed for the larger Ba^{2+} cation which only occupies the Yb2 and Yb4 sites. Ca and Yb occupy the remaining sites. The final refined composition is very close to that obtained by EMPA (Table 1). The cation site occupancy is shown graphically in Figure 2 and provided as factional occupancy in Table S2. Figure 2 also shows the polyhedra for the four Yb sites and their relationship to the

tetrahedra and Sb_3 linear anion, along with a partial view of the unit cell showing a portion where all polyhedral are indicated. The volume of the unit cell (6142(1) $Å^3$) is larger than that of $Yb_{14}MgSb_{11}$ which is also shown to contain Yb^{3+} (6079(2) $Å^3$)[29] but smaller than that of $Ca_{14}MgSb_{11}$ (6291(2) $Å^3$).[19] The Ba and Ca incorporation increase the size of the unit cell, as expected.

Table S4 provides a comparison of the single crystal bond lengths and angles with $Yb_{14}MgSb_{11}$.[29] The A-Sb (A = Yb/Ca/Ba) bond lengths are larger when compared to the reported crystal structure of $Yb_{14}MgSb_{11}$ which also shows a similar amount of Mg^{2+} in the octahedral A sites.[29] In $Yb_{14-x}Ca_xMnSb_{11}$, lengthening in A-Sb is observed and attributed to Ca ionizing more completely compared to Yb causing bond elongation and decreasing carrier concentration.[42] While A-Sb elongation is seen, contraction in distance in the Sb(1)-Sb(4) linear unit's distance is not seen showing the differences between the Mg/Mn system and with the additional Ba incorporation. The angles of the $MgSb_4$ tetrahedron are also about the same as those for in $Yb_{14}MgSb_{11}$.

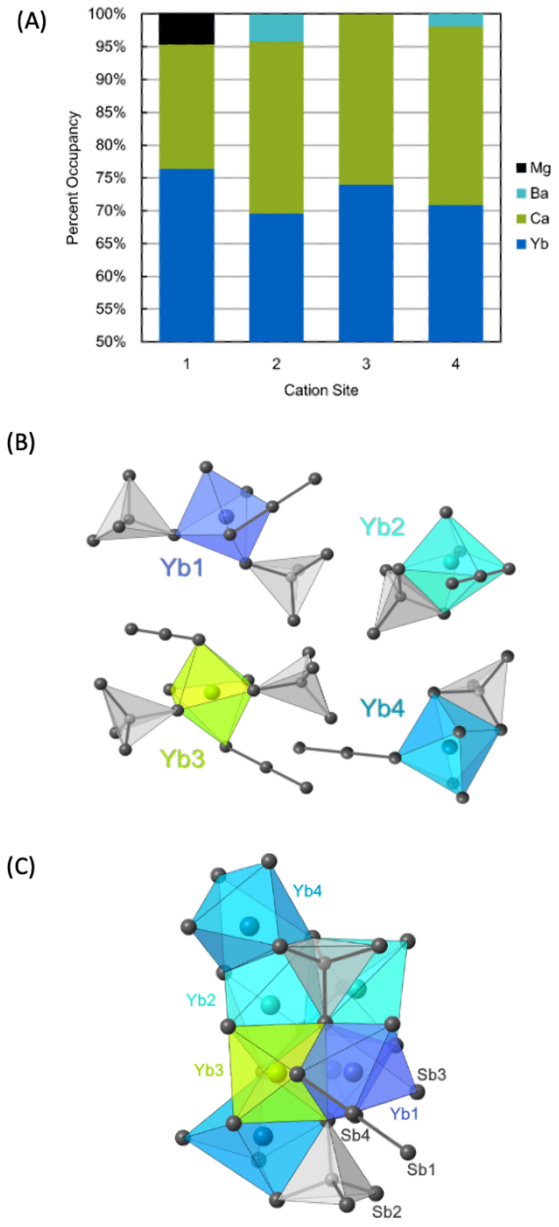

Figure 2: Site occupancy of Yb1, Yb2, Yb3, and Yb4 obtained from single crystal X-ray refinement of $Yb_{10.15}Ca_{3.42}Ba_{0.25}Mg_{1.18}Sb_{11}$. The chart starts at 50% to amplify the Mg and Ba fractions which are minimal (A). Views of the 4 Yb polyhedral with the Sb_3 linear units and $MgSb_4$ tetrahedra indicated (B). The four octahedral Yb sites illustrated together as polyhedra with two $MgSb_4$ tetrahedra and a Sb_3 linear anion (Sb1-Sb4-Sb1) in a selection taken from the unit cell (C).

Table 1: Single Crystal Data Collection and Refinement Parameters for $Yb_{10.15}Ca_{3.42}Ba_{0.25}Mg_{1.18}Sb_{11}$

Parameters	
Crystal Dimensions (mm)	0.15 x 0.11 x 0.060
Empirical formula	$Yb_{10.15}Ca_{3.42}Ba_{0.25}Mg_{1.18}Sb_{11}$
Molar Mass (g mol^{-1})	3295.92
Crystal system	Tetragonal
Space group	$I4_1/acd$ (no. 142)
Temperature (K)	90
Radiation λ (Å)	0.71073
Z	8
a (Å)	16.6247(15)
b (Å)	22.222(2)
V ($Å^3$)	6141.7(13)
ρ_{calc} (g cm^{-3})	7.129
Abs. coeff. μ (mm^{-1})	40.948
Reflns./Indep. Reflns.	45076/2247
Parameters refined	62
GOF on F^2	1.183
R indices [I > 2σ(I)]	R_1 = 0.0199, wR_2 = 0.0435
R indices (all data)	R_1 = 0.0208, wR_2 = 0.0438

3.2 Magnetism. Figure 3 provides the χ vs T and $1/\chi$ vs T plots acquired on a single crystal characterized by EMPA to give $Yb_{9.7(2)}Ca_{3.85(5)}Ba_{0.29(4)}Mg_{1.13(3)}Sb_{11.0(1)}$. The $1/\chi$ data were fit from 125 to 300 K with the Curie-Weiss law (eq. 11) where *C* is the Curie constant and θ is the Weiss constant. The effective moment, μ_{eff}, was calculated with eq. 12 and yielded values of μ_{eff} = 4.2(1) μ_B and θ = 89 K. Yb^{3+} (f^{13}) is the only potentially magnetic species, and 1 Yb^{3+} has an expected magnetic moment of 4.5 μ_B. Therefore ~0.85 Yb^{3+} are present per formula unit which is in line with what is reported in literature for $Yb_{14}MgSb_{11}$ (0.8 Yb^{3+}).[29, 43]

$$\chi(T) = \left(\frac{C}{T-\theta}\right) \quad (11), \quad \mu_{eff} = \sqrt{8C} \quad (12)$$

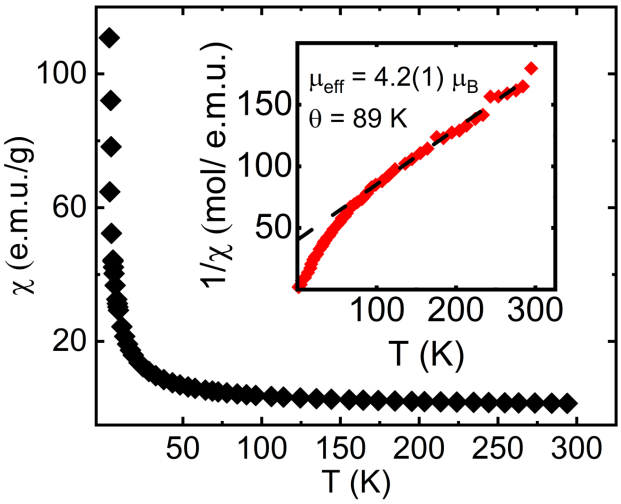

Figure 3: χ vs T measured on a single crystal of $Yb_{9.7(2)}Ca_{3.85(5)}Ba_{0.29(4)}Mg_{1.13(3)}Sb_{11.0(1)}$. The inset shows 1/ χ vs T (data in red) with the high temperature fit (black dashed line). A picture of the parent crystal is shown in SI, Figure S4.

3.3 Structure and composition of $Yb_{13-x}Ca_xBaMgSb_{11}$ polycrystalline samples. Table 2 summarizes the calculated composition from EMPA of the pressed pellets. The Mg amount is close to the expected stoichiometry consistent with Mg in the tetrahedron and varies from 1.02(1) to 0.97(2). These compositions suggest that when prepared *via* metallurgical synthesis Mg is not substituted on the octahedral Yb sites, as is noted for the single crystals obtained from Sn flux.[29, 43] As the Ca amount increases, Sb systematically goes from close to nominal composition to deficient. The overlap in Ca's $K\alpha_1$ and Sb's $L\beta_1$ which are 3.69 eV and 3.66 eV, respectively; leads to some Sb signal being attributed to Ca. Yb and Ba could be slightly deficient due to adherence of these malleable elements to the mill container as previously mentioned in the literature.[16] Overall, the observed compositions of these quinary phases are close to the nominal composition and the $Yb_{13-x}Ca_xBaMgSb_{11}$ samples will be referred to according to their nominal composition, *x*.

Table 2: Nominal vs Measured Stoichiometry from EMPA.

$Yb_{13-x}Ca_xBaMgSb_{11}$	EMPA stoichiometry
$x = 1$	$Yb_{11.84(4)}Ca_{1.14(2)}Ba_{0.98(1)}Mg_{1.02(1)}Sb_{11.00(4)}$
$x = 2$	$Yb_{10.94(3)}Ca_{2.19(2)}Ba_{0.97(2)}Mg_{0.93(2)}Sb_{10.97(4)}$
$x = 3$	$Yb_{9.93(8)}Ca_{3.19(2)}Ba_{0.98(2)}Mg_{0.93(2)}Sb_{10.96(6)}$

$x = 4$	$Yb_{8.87(4)}Ca_{4.25(2)}Ba_{0.97(1)}Mg_{1.00(2)}Sb_{10.92(3)}$
$x = 5$	$Yb_{7.90(3)}Ca_{5.31(3)}Ba_{0.97(2)}Mg_{0.96(2)}Sb_{10.87(4)}$
$x = 6$	$Yb_{6.91(9)}Ca_{6.32(4)}Ba_{0.97(1)}Mg_{0.97(1)}Sb_{10.83(6)}$

Figure 4 shows normalized PXRD patterns for $Yb_{13-x}Ca_xBaMgSb_{11}$ (x = 1 – 6) after SPS. The CIF obtained from the single crystal structural solution described in sections 2.4 and 3.1 was used to generate the $A_{14}MPn_{11}$ model for Rietveld refinement. Cation occupancies were modified using acquired EMPA compositions (Table 2) restricting Mg to the tetrahedral site and Ba to the Yb2 and Yb4 sites. Yb and Ca were distributed equally across the cation sites according to their EMPA compositions and Ba was distributed equally across the Yb2 and Yb4 sites. This allocation was performed to reduce issues with refining 3 or more atoms on one site with Rietveld refinement. While this allocation of the cation sites could lead to higher wR_p and GOF values, the generated model matches the data well providing wR_p values of about 10% indicating a good refinement model and high sample purity (PXRD refinements are provided in SI, Figure S1, with the lattice parameters and unit cell volume, refinement parameters summarized in Table 3). Some samples have a reflection (denoted with *) at 27.1˚ 2θ attributed to an unidentified impurity. Phase matching for any of the cation oxide phases and cation-Sb binary phases does not match this reflection. There is a ~1 mass % Yb_2O_3 impurity in the samples denoted by Δ which may be due to surface oxidation as reported in literature.[16] Yb_2O_3 does not refine well for the x = 5, 6 samples, suggesting that it is not present. The $Yb_{11}Sb_{10}$ phase, a common impurity, does not refine well, and the phase's main reflections at ~31.4 and ~32.0˚ 2θ are missing suggesting that this impurity is not present and indicating that the MgH_2 precursor allows for good dispersion of Mg. A good dispersion of MgH_2 throughout the powder provides a final high purity material (≥ 98 %) with very little oxide or $Yb_{11}Sb_{10}$.

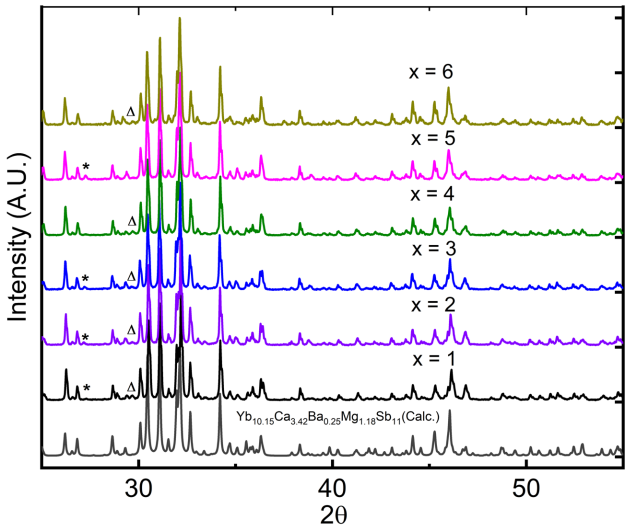

Figure 4: Simulated and collected/normalized PXRD data for $Yb_{13-x}Ca_xBaMgSb_{11}$ (x = 1 – 6). * denotes a reflection attributed to a minor unidentified impurity and Δ denotes the major reflection for Yb_2O_3, present in amounts ≤ 1.3 mass %.

Table 3: Results of PXRD Rietveld Refinement for $Yb_{13-x}Ca_xBaMgSb_{11}$

$Yb_{13-x}Ca_xBaMgSb_{11}$	a (Å)	c (Å)	V (Å^3)	Yb_2O_3 (wt. %)	wRp (%)	GOF
x = 1	16.785(4)	22.241(7)	6266.4(3)	1.31(13)	10.38	2.18
x = 2	16.790(4)	22.258(7)	6275.4(3)	0.86(12)	11.58	2.25
x = 3	16.796(4)	22.278(8)	6284.8(3)	0.53(7)	10.84	2.21
x = 4	16.794(7)	22.29(1)	6286.7(7)	1.22(9)	12.66	2.42
x = 5	16.785(4)	22.322(9)	6289.2(3)	N/A	11.98	2.41
x = 6	16.784(6)	22.33(1)	6290.7(5)	N/A	13.6	2.25

Figure 5 shows the unit cell volume (determined by Rietveld refinement and listed in Table 3) as a function of Ca content. The unit cell increases as a function of Ca from x = 1 to x = 3 after which the volume still increases but not at the same rate. Since there is site preference of the cation substitution with Ba occupying Yb2/Yb4 and Ca occupying all sites, it is not clear that the unit cell volume should follow a simple linear function as is the case for Vergard's law. It would be useful to grow single crystals of the series to better understand the changes in the unit cell. The unit cell expansion is expected to improve the thermoelectric performance in the following way: peak thermoelectric performance in $Yb_{14}MSb_{11}$ (M = Mn, Mg) is seen above 1200 K where the unit cell has expanded by up to 1.6% (98 Å^3 in $Yb_{14}MgSb_{11}$).[19, 21] The $Yb_{12}CaBaMgSb_{11}$ composition with the smallest unit cell of the series, has a volume of

6266.4(3) Å^3 is already larger than the projected unit cell volume of $Yb_{14}MgSb_{11}$ at 1200 K (6243 Å^3).

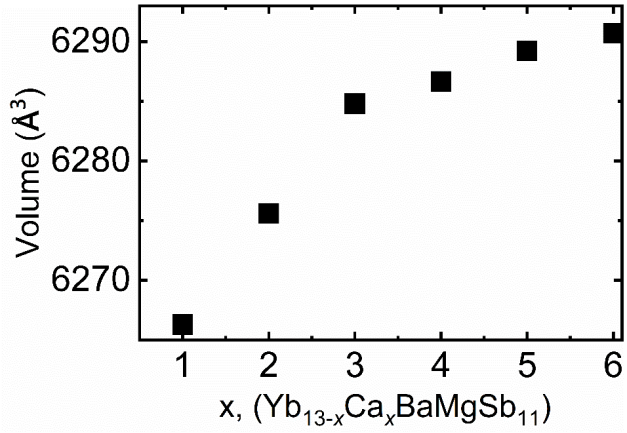

Figure 5: Unit cell volume vs. Ca content, *x*, for $Yb_{13-x}Ca_xBaMgSb_{11}$.

3.3 Hall effect. Figure 6A shows the hole carrier concentration (n_H) and Hall mobility (μ_{Hall}) vs. temperature. At room temperature Ca has the effect of decreasing the overall magnitude of a sample's carrier concentration(Figure S5), previously documented in $Yb_{14-x}Ca_xMnSb_{11}$.[42] This effect is observed in other Zintl phases as well and has be attributed to either reduction of cation defects with the substitution of Ca or to changes in bonding as the polar covalent Yb-Sb bond is replaced by the ionic Ca-Sb bond.[19, 44] A unique feature of Ca substitution for this solid solution series is that at temperatures > 600 K the relative order of carrier concentration changes, with increased Ca concentration resulting in higher carrier concentration and a steeper increase, most notable for x = 4-6. At the highest temperatures (>1100 K) this increase is attributed to the activation of minority carriers known as bipolar conduction, which reduces the sample's measured hall voltage. As described in the introduction, the band structures of all of these phases are similar, but there are small differences in position of the bands.[22] With increasing Ca and temperature electrons may be activated into an empty localized state leaving behind a more mobile hole in the valence band and thereby generating an increase of the charge carrier concentration with temperature. This state could be a localized nonbonding Sb or defect state or could be consequences of the electronic differences between Yb and Ca atoms, and therefore the different energetic level occupancy. A localized nonbonding state for the Sb_3^{7-} unit is found close to the Fermi level in

related analogs.[22, 23] The *f*-states of Yb are embedded deeper in the valence band and therefore they should not have a strong influence on the DOS close to the Fermi level.[22] On the contrary, Ca states are present close the top of the valence band and at the bottom of the conduction band in the reported band structures, and therefore they have a larger contribution to the overall DOS.[19, 22] More examples of this phenomena in other compounds of this structure type along with theoretical calculations are necessary to better understand the increase in carrier concentration above 600 K. Regardless of the mechanism for the change in carrier concentration with temperature, carrier mobility is inversely proportional to the trend of carrier concentration as expected.

Figure 6B shows the carrier concentration at 900 K and the effective mass (m^*) calculated as in literature[45] using experimental Hall effect data, Seebeck, and electrical conductivity. As the carrier concentration increases, the Fermi level gets pushed down from the lighter (Γ) VB_1 band to the heavier VB_2 (N-P, as shown in the inlay of Figure 6B) and as a result the effective mass increases. The heavier VB_2 (N-P) band is credited with the high thermoelectric performance of $Yb_{14}MgSb_{11}$ due to a high valley degeneracy, $N_V = 8$, indicating that the samples with higher carrier concentration could have the highest zT.[22]

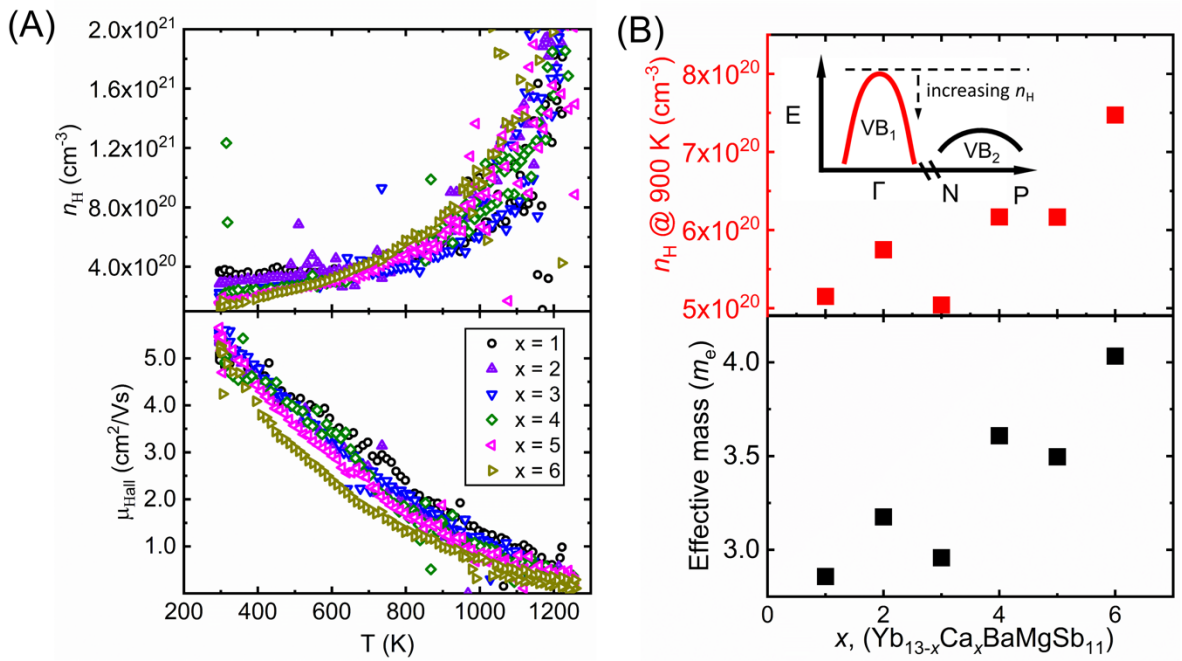

Figure 6: Carrier concentration (n_H) and Hall mobility (μ_{Hall}) vs temperature for $Yb_{13-x}Ca_xBaMgSb_{11}$ (A). The carrier concentration vs Ca content (B) shows at 900 K as carrier concentration increases the effective mass increases (B). The inlay shows a schematic of the simplified model band model.[22] As the carrier concentration of the *p*-type material increases the system moves from the light (Γ) band to the heavy high valley degeneracy (N-P) band as shown by the increasing effective mass.

3.4 Seebeck. Figure 7A shows the Seebeck coefficients vs temperature for $Yb_{13-x}Ca_xBaMgSb_{11}$ in which the values do not show the downturn at 1200 K as seen in the $Yb_{14}MgSb_{11}$ system.[9, 16] This could be due to an expanding bandgap as a result of Ca and Ba incorporation. The Goldsmid and Sharp expression ($E_g = 2e|S_{max}|T_{max}$) cannot be used to calculate the band gap in this system as there is no Seebeck maxima; however, it does seem that the Seebeck values have plateaued at 1273 K in all samples so, it is logical to conclude that the band gap of the x = 1 – 6 samples are larger than $Yb_{14}MgSb_{11}$ as S_{max} and T_{max} are larger (avg: 236 μV/K, 1273 K for x = 1 – 6, avg: ~0.61 eV) (232 μV/K, 1200 K for $Yb_{14}MgSb_{11}$, 0.56 eV).[46] Another mechanism that is suppressing bipolar conduction could be a result of an increase in carrier concentration seen in Figure 6. As the carrier concentration is

increased, the Fermi level moves down as stylized in Figure 6B making the promotion of electrons from the valence band to the conduction band less likely as was observed in K doped PbTe.[17, 18] Assuming a single parabolic band model, the systematic increase in carrier concentration shown in Figure 6B should lead to a decrease in Seebeck coefficient, but at ~1100 K, all of the Seebeck values converge. This deviation from a single parabolic band model is emphasized by the Pisarenko plot (Figure 7B) which shows that as carrier concentration increases the Seebeck coefficient does not decrease. Instead, the transport is dominated by a heavier band as recently described for $Yb_{14}Mg_{1-x}Al_xSb_{11}$ with a three-band model where the valence bands are stylized in Figure 6B.[22] In this model, as carrier concentration increases, transport changes from the lighter Γ (VB_1) band to the highly degenerate N_V = 8 N-P (VB_2) band which allows sustained Seebeck coefficients at high carrier concentrations (n_H> 10^{21}) which is reflected in this system.

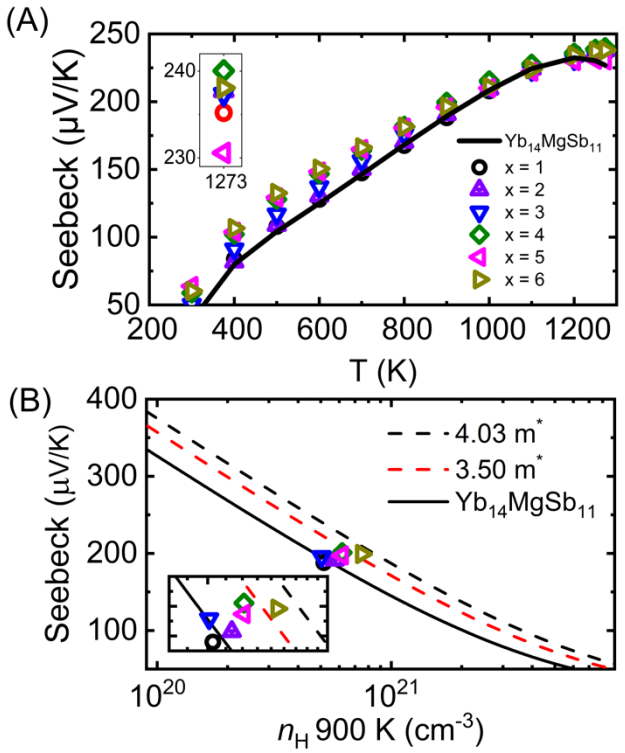

Figure 7: Seebeck coefficient vs. temperature for $Yb_{13-x}Ca_xBaMgSb_{11}$ (x = 1 – 6) compared with $Yb_{14}MgSb_{11}$ data from literature.[9] The inlay show the peak values at 1273 K (A). The Pisarenko plot with inlay of an expanded region (B) shows the transport at 900 K is not

dominated by a single band, instead as the carrier concentration increases the transport switches from a lighter (Γ) to a heavier band (N-P) with the line for $x = 0$.[22] The legend for (A) applies to (B).

3.5 Electrical resistivity: The electrical resistivity for $Yb_{13-x}Ca_xBaMgSb_{11}$ is shown in Figure 8. Low Ca amounts follow the same slope and trend for resistivity of $Yb_{14}MgSb_{11}$, but as the amount of Ca increases above $x = 4$, the temperature dependence changes. The temperature trend of the resistivity for $x > 4$ compositions is more similar to that reported for $Ca_{14}MgSb_{11}$ at lower temperatures, and to $Yb_{14}MgSb_{11}$ at higher temperatures.[19] The temperature dependence of $x = 4, 5, 6$ samples is not likely due to differences in microstructure as SEM images (Figure S6) show the microstructures of the samples are roughly equivalent. The temperature dependent behavior can be explained by the lower carrier concentration below 600 K and the rapid increase in carrier concentration at temperatures above 600 K seen in the $x > 4$ samples (Figure S5 vs Figure 6B). Overall, the resistivity for all samples converges around 9 mΩ cm at 1273 K. Interestingly, despite having larger carrier concentrations and lower mobilities than the $x = 1 – 3$ samples above ~600 K, the $x = 4 – 6$ samples are not significantly more conductive which may be attributed to increased electron scattering as a result of Ca incorporation.

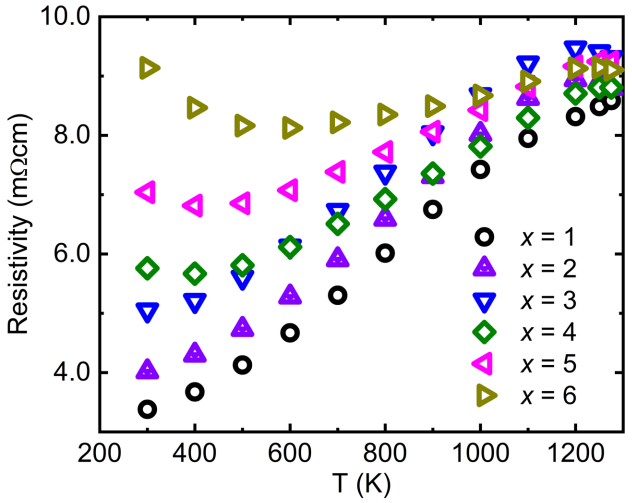

Figure 8: Resistivity vs temperature for $Yb_{13-x}Ca_xBaMgSb_{11}$.

3.6 Physical properties. The density of the samples is at least 99% of the density predicted

from EMPA and lattice parameters (Figure 9). The density decreases linearly as a function of Ca content as expected. From an application point of view, the reduction in density can be seen as a favorable aspect, since lighter materials capable of generating the same power output of the heavier counterpart, will have in the end a higher specific power density (W/Kg). This is a crucial aspect for several applications and specially for space applications, where each Kg of mass of the spacecraft costs up to several tens of thousands of dollars. The shear speed of sound increases linearly as a function of Ca until $x = 4$ and then tends to flatten, while the longitudinal speed of sound increases linearly over the whole compositional range. These changes are consistent with the trend seen in Figure 5 for the volume of the unit cell. The shear and Young modulus show that the lattice is becoming stiffer as we increase the amount of the more ionic Ca^{2+} cation (replacing Yb) until $x = 3$, then the lattice slightly softens for $x = 4$ and $x = 5$ before increasing again for $x = 6$. In the end, all samples are stiffer (higher Young's modulus) than $Yb_{14}MgSb_{11}$ (64.45 GPa).[16] As a lattice stiffens, κ_l typically increases, therefore κ_l would be expected to increase if not for the alloy scattering induced by the introduction of Ca.[47] A more detailed discussion of the thermal conductivity can be found in the next section.

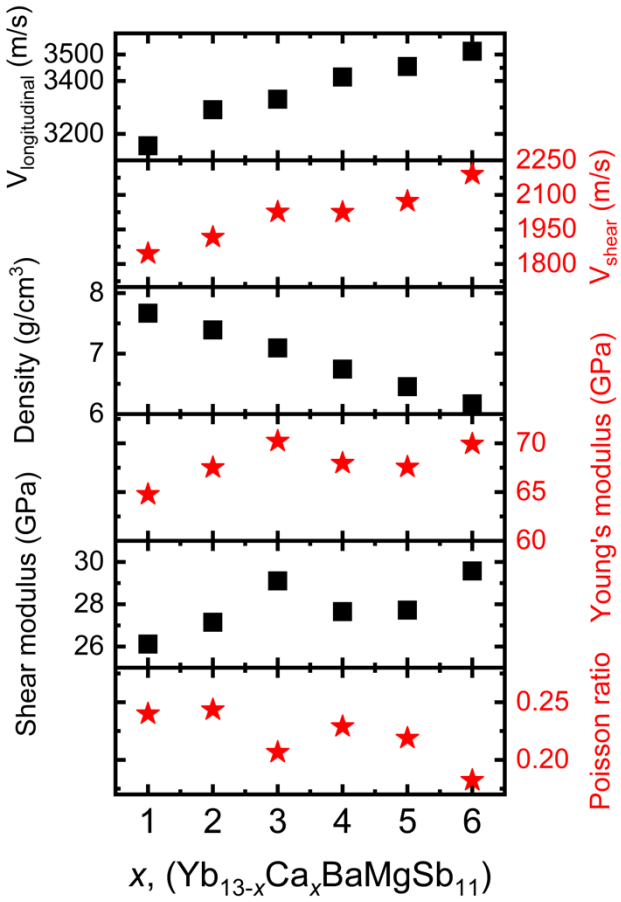

Figure 9: $V_{longitudinal}$, V_{shear}, density, Young's modulus, Shear modulus, and Poisson ratio vs. Ca content, x, for $Yb_{13-x}Ca_xBaMgSb_{11}$ samples.

3.7 Thermal conductivity. κ_{tot} and κ_l were calculated as stated in section 2.12 and are shown in Figure 10. All compositions of $Yb_{13-x}Ca_xBaMgSb_{11}$ have lower κ_{tot} and κ_l than that of $Yb_{14}MgSb_{11}$ at high temperatures except $x = 6$. There are three important contributions that are described below.

The first item of note is the low temperature (< 600 K) thermal conductivity. As previously shown in the $Yb_{14}Mg_{1-x}Al_xSb_{11}$ system,[22] the initial increase in thermal conductivity in $Yb_{14}MgSb_{11}$ observed up to ~450 K is due to carrier excitation from the VB_1 to VB_2 (NP) band causing a maximum in the thermal conductivity. As carrier concentration decreases in the $Yb_{14}Mg_{1-x}Al_xSb_{11}$ system the magnitude of the effect is diminished and the maxima moves to higher temperatures. As previously discussed (Figure S5), at low temperatures (< 600 K) the

carrier concentration decreases with increasing Ca. Qualitatively, Figure 10 shows the magnitude of the low temperature increase is diminished as a function of Ca and Figure S7 shows the maxima seen in $Yb_{14}MgSb_{11}$ shifts to higher temperatures as a function of Ca content via the first derivative of κ_{tot} vs temperature, < 650 K, $x = 0 – 4$, ($x = 5, 6$ is not shown as no low temperature transition is observed) supporting the 3 band model with carriers from VB_2 accounting for the maximum observed in the thermal conductivity.

Next, we discuss the effect Ca incorporation has on high temperature bipolar conduction. Typically, the κ_{tot} for $Yb_{14}MgSb_{11}$ and $Yb_{14}MnSb_{11}$ shows a dramatic increase above 1200 K due to bipolar conduction (Figure 10), but this effect is reduced in $x = 1 – 4$ samples and eliminated in $x = 5, 6$ samples. Along with the Seebeck data, it is clear that the increased carrier concentration and larger bandgap are mitigating bipolar conduction at the highest temperatures. These results lay the groundwork for further improvements of the thermoelectric performance of compositions of the 14-1-11 family of compounds.

Lastly, we discuss the alloy scattering effect. κ_l decreases as a function of Ca incorporation, and is at its lowest at $x = 3, 4$ then increases for the $x = 5, 6$ samples. These changes with x may indicate that the alloy scattering has the maximum effect at $x = 3, 4$ and in the case of the $x = 5, 6$ samples, the lattice has become too stiff to benefit from additional alloy scattering. Compositions with $x = 3, 4$ have the best combination of alloy scattering without being affected by the stiffening lattice which result in very low κ_l and κ_{tot}.

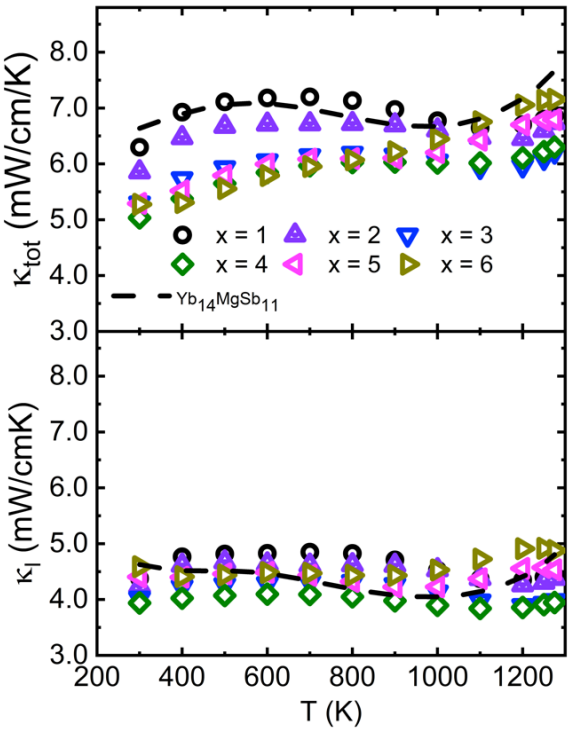

Figure 10: κ_{tot} and κ_l vs. temperature for $Yb_{13-x}Ca_xBaMgSb_{11}$ (x = 1-6) compared with $Yb_{14}MgSb_{11}$ data from literature.[9]

3.8 ***zT.*** Figure 11A shows *zT* as a function of composition for $Yb_{13-x}Ca_xBaMgSb_{11}$. The *zT* of the x = 4 sample results in a peak *zT* of 1.32 which is higher than the previous maxima reported for $Yb_{14}MgSb_{11}$ (1.26) and the first example of an analog that competes with $Yb_{14}MnSb_{11}$ (1.35).[8, 9] The integrated ZT_{avg} (eq. 13) from 873 to 1273 K (the proposed operational range for 14-1-11 based RTGs) is 1.07 for x = 4. This value is about the same as the integrated *ZT's* for $Yb_{14}MnSb_{11}$ and $Yb_{14}MgSb_{11}$ indicating that this material can perform with state of the art materials while being 16% lighter by molar mass providing a much higher power density.[8, 15, 48] Additionally, this method of optimization can be employed with additional strategies such as carrier concentration tuning, band consolidation, and compositing to further improve the *zT*.[7, 16, 30, 35, 49] Ultimately, the x = 1 - 6 samples all have *zT's* that are within 17% of the best reported for $Yb_{14}MnSb_{11}$ and within the accepted 20% error in measurement[50] giving a wider range of thermal and electrical properties that are important when designing a thermoelectric generator.

$$\frac{1}{\Delta T}\int_{T_c}^{T_h} z(T)\, dT \quad (13)$$

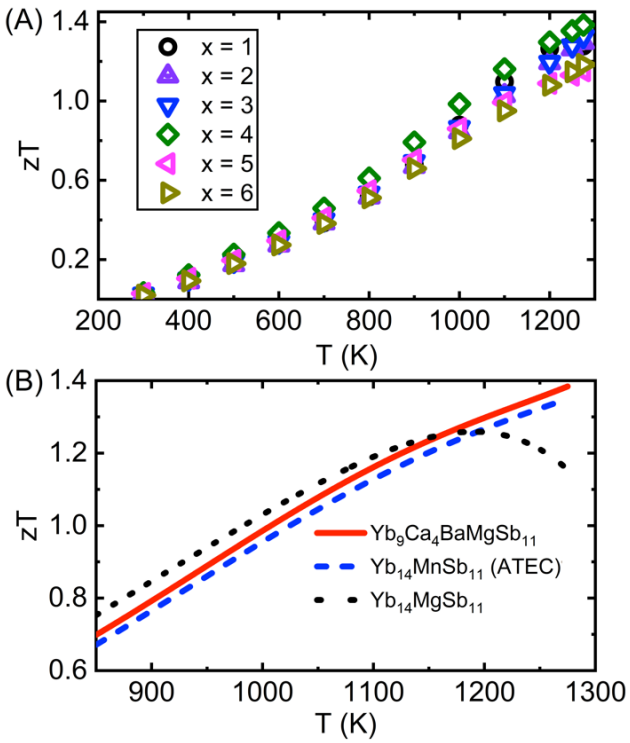

Figure 11: zT vs temperature for $Yb_{13-x}Ca_xBaMgSb_{11}$ (A), and zT of $Yb_9Ca_4BaMgSb_{11}$ compared to the highest reported zT for the 14-1-11 structure type (data from literature)[8, 9] (B).

4. Conclusion. Single crystals of $Yb_{13-x}Ca_xBaMgSb_{11}$, x ~4, were grown from a Sn flux for structural and magnetic investigations. Single crystal refinement shows that Mg partially occupies the Yb1 site, Ba occupies the Yb2 and Yb4 sites while Yb and Ca occupy all four Yb sites in the 14-1-11 structure. Magnetic measurements on this crystal indicate that ~0.85 Yb^{3+} is present, similar to what has been reported for $Yb_{14}MgSb_{11}$.[29] Bulk samples of $Yb_{13-x}Ca_xBaMgSb_{11}$ were metallurgically synthesized. EMPA of the bulk samples show that the x = 1 - 6 samples closely follow nominal stoichiometry with Mg only on the tetrahedral site. PXRD is consistent with the structural model from single crystal refinement and show >98 % pure phase samples with expansion of the unit cell as a function of increasing Ca content. The carrier concentration increases dramatically at temperatures > 600 K for the x = 4 – 6 samples which may be attributed to filling of a localized Sb state or defect state. This is the first example where this effect has been document for compounds of the 14-1-11 structure and merits further investigation with other cations and theory. The Seebeck coefficient does not show a significant difference for any of the samples at the highest temperatures (> 1000 K) indicating that the

samples are transitioning from a light Γ band (VB_1) to a heavy, highly degenerate N-P band (VB_2) which allows for sustained Seebeck coefficients. The increasing carrier concentration and expanding band gap of $Yb_{13-x}Ca_xBaMgSb_{11}$ are credited with the disappearance of bipolar conduction (> 1000 K) observed in $Yb_{14}MgSb_{11}$. The temperature dependence of the resistivity for the $x = 4 – 6$ samples is semiconducting in nature at low temperatures and metallic at high temperatures and is within 2 mΩcm for all samples at 1273 K. Speed of sound measurements show that the lattice becomes stiffer with substitution of Yb for the more ionic Ca cation. As a result, the lowest κ_l is not seen in the $x = 6$ sample which has the stiffest lattice. The $x = 3$ and 4 samples have the lowest κ_l and κ_{tot} due to a combination of significant alloy scattering and minimum lattice stiffening. Thermal conductivity measurements also show the mitigation of bipolar conduction at > 1200 K with increasing Ca. The low κ_{tot} of the $x = 4$ sample leads to a zT of 1.32 with a 16% weight reduction compared to $Yb_{14}MnSb_{11}$. This aspect is of fundamental importance, especially for space applications, where such reduction in weight can translate in a reduction of launch costs of several tens of thousands of dollars. Furthermore, this work gives a wide range of 14-1-11 compounds with excellent zT's that can be chosen for desired thermal or electrical properties for optimal segmented thermoelectric devices.[51]

5. Associated content. Additional crystallographic data for $Yb_{10.15}Ca_{3.42}Ba_{0.25}Mg_{1.18}Sb_{11}$ in CIF file format is attached; a table of EMPA data before and after calculations, a table containing atomic coordinates and equivalent isotropic and anisotropic displacement parameters, plots of Rietveld refinement for polycrystalline samples, and plots of experimental Seebeck, thermal diffusivity, and resistivity data, the parent crystal for structural and magnetic studies, carrier concentration vs Ca content at 300 K, SEM of the samples studied, and analysis of the onset of low temperature bipolar conduction (PDF). This material is free of charge and available at http://pubs.acs.org.

6. Author information. Corresponding Author's* e-mail: smkauzlarich@ucdavis.edu. ORCID Christopher J. Perez: 0000-0002-1088-0190, Giacomo Cerretti: 0000-0001-5258-1589, Elizabeth L. K. Wille: 0000-0002-2806-2663, Kasey P. Devlin: 0000-0002-2633-7029, Navtej S. Grewal: 0000-0002-6892-0394, Andrew P. Justl: 0000-0001-6332-4545, Maxwell Wood: 0000-0003-2758-6155, Sabah K. Bux: 000-0002-5372-354X, Susan M. Kauzlarich:

0000-0002-3627-237X

7. Acknowledgments. This work was supported by NEUP, NSF DMR-1709382, DMR-2001156, and the NASA Science Missions Directorate's Radioisotope Power Systems Program. This work was performed in part at the Jet Propulsion Laboratory, California Institute of Technology under contract with the National Aeronautics and Space Administration. The authors thank Valentin Taufour for access to the MPMS for magnetic measurements, Dr. Chi Ma for help acquiring EMPA data and Dr. Dean Cheikh for relevant heat capacity and physical property discussion. G. Cerretti's and M. Wood's research at the Jet Propulsion Laboratory was supported by an appointment to the NASA Postdoctoral Program, administered by Universities Space Research Association under contract with NASA.

8. **References.**

1. Fernández-Yáñez, P.; Romero, V.; Armas, O.; Cerretti, G., Thermal management of thermoelectric generators for waste energy recovery. *Appl. Therm. Eng.* **2021,** *196,* 126102.
2. Baranowski, L. L.; Snyder, G. J.; Toberer, E. S., The misconception of maximum power and power factor in thermoelectrics. *J. Appl. Phys* **2014,** *115*, 126102.
3. Snyder, G. J.; Toberer, E. S., Complex thermoelectric materials. *Nat. Mater.* **2008,** *7* (2), 105-114.
4. Shi, X.; Yang, J.; Salvador, J. R.; Chi, M.; Cho, J. Y.; Wang, H.; Bai, S.; Yang, J.; Zhang, W.; Chen, L., Multiple-filled skutterudites: high thermoelectric figure of merit through separately optimizing electrical and thermal transports. *J. Am. Chem. Soc.* **2011,** *133* (20), 7837-46.
5. Shuai, J.; Geng, H.; Lan, Y.; Zhu, Z.; Wang, C.; Liu, Z.; Bao, J.; Chu, C. W.; Sui, J.; Ren, Z., Higher thermoelectric performance of Zintl phases $(Eu_{0.5}Yb_{0.5})_{1-x}Ca_xMg_2Bi_2$ by band engineering and strain fluctuation. *Proc. Natl. Acad. Sci. U. S. A.* **2016,** *113* (29), E4125-32.
6. Kauzlarich, S. M.; Zevalkink, A.; Toberer, E.; Snyder, G. J., Chapter 1. Zintl Phases: Recent Developments in Thermoelectrics and Future Outlook. In *Thermoelectric Materials and Devices*, The Royal Society of Chemistry: 2016; pp 1-26.
7. Hu, Y. F.; Cerretti, G.; Wille, E. L. K.; Bux, S. K.; Kauzlarich, S. M., The remarkable crystal chemistry of the $Ca_{14}AlSb_{11}$ structure type, magnetic and thermoelectric properties. *J. Sol. State Chem.* **2019,** *271*, 88-102.
8. Grebenkemper, J. H.; Hu, Y. F.; Barrett, D.; Gogna, P.; Huang, C. K.; Bux, S. K.; Kauzlarich, S. M., High Temperature Thermoelectric Properties of $Yb_{14}MnSb_{11}$ Prepared from Reaction of MnSb with the Elements. *Chem. Mater.* **2015,** *27* (16), 5791-5798.
9. Justl, A. P.; Cerretti, G.; Bux, S. K.; Kauzlarich, S. M., Hydride assisted synthesis of the high temperature thermoelectric phase: $Yb_{14}MgSb_{11}$. *J. Appl. Phys.* **2019,** *126* (16), 165106.
10. Kim, H.; Olmstead, M. M.; Klavins, P.; Webb, D. J.; Kauzlarich, S. M., Structure, Magnetism, and Colossal Magnetoresistance (CMR) of the Ternary Transition Metal Solid Solution Ca14-xEuxMnSb11 ($0 < x < 14$). *Chem. Mater.* **2002,** *14*, 3382-3390.
11. Kim, H.; Klavins, P.; Kauzlarich, S. M., Structure, Magnetism, and Magnetoresistance of

the Rare-Earth Transition Metal Compounds $Eu_{13}AMnSb_{11}$ (A = Ca, Sr, Ba, and Yb). *Chem. Mater.* **2002,** *14*, 2308-2316.
12. Vasilyeva, I. G.; Nikolaev, R. E.; Abdusaljamova, M. N.; Kauzlarich, S. M., Thermochemistry study and improved thermal stability of $Yb_{14}MnSb_{11}$ alloyed by Ln^{3+} (La–Lu). *J. Mater. Chem. C* **2016,** *4* (15), 3342-3348.
13. Prakash, J.; Stoyko, S.; Voss, L.; Bobev, S., On the Extended Series of Quaternary Zintl Phases $Ca_{13}REMnSb_{11}$ (RE = La–Nd, Sm, Gd–Dy). *Eur. J. Inorg. Chem.* **2016,** *2016* (18), 2912-2922.
14. Nam, G.; Jang, E.; Jo, H.; Han, M. K.; Kim, S. J.; Ok, K. M.; You, T. S., Cationic Site-Preference in the $Yb_{14-x}Ca_xAlSb_{11}$ ($4.81 \leq x \leq 10.57$) Series: Theoretical and Experimental Studies. *Materials (Basel)* **2016,** *9* (7), 553.
15. Fleurial, J. P., Thermoelectric Power Generation Materials: Technology and Application Opportunities. *JOM* **2009,** *61* (4), 79-85.
16. Perez, C. J.; Qi, X.; Chen, Z. J.; Bux, S. K.; Chanakain, S.; Li, B.; Liu, K.; Dhall, R.; Bustillo, K. C.; Kauzlarich, S. M., Improved Power Factor and Mechanical Properties of Composites of $Yb_{14}MgSb_{11}$ with Iron. *Acs Appl Energ Mater* **2020,** *3* (3), 2147-2159.
17. Wu, H. J.; Zhao, L. D.; Zheng, F. S.; Wu, D.; Pei, Y. L.; Tong, X.; Kanatzidis, M. G.; He, J. Q., Broad temperature plateau for thermoelectric figure of merit ZT>2 in phase-separated $PbTe_{0.7}S_{0.3}$. *Nat. Commun.* **2014,** *5* (1), 4515.
18. Girard, S. N.; He, J.; Zhou, X.; Shoemaker, D.; Jaworski, C. M.; Uher, C.; Dravid, V. P.; Heremans, J. P.; Kanatzidis, M. G., High Performance Na-doped PbTe–PbS Thermoelectric Materials: Electronic Density of States Modification and Shape-Controlled Nanostructures. *J. Am. Chem. Soc.* **2011,** *133* (41), 16588-16597.
19. Hu, Y.; Wang, J.; Kawamura, A.; Kovnir, K.; Kauzlarich, S. M., $Yb_{14}MgSb_{11}$ and $Ca_{14}MgSb_{11}$—New Mg-Containing Zintl Compounds and Their Structures, Bonding, and Thermoelectric Properties. *Chem. Mater.* **2014,** *27* (1), 343-351.
20. Rehr, A.; Kuromoto, T. Y.; Kauzlarich, S. M.; Del Castillo, J.; Webb, D. J., Structure and properties of the transition-metal Zintl compounds $A_{14}MnPn_{11}$ (A = Ca, Sr, Ba; Pn = As, Sb). *Chem. Mater.* **1994,** *6* (1), 93-99.
21. Ravi, V.; Firdosy, S.; Caillat, T.; Brandon, E.; Van der Walde, K.; Maricic, L.; Sayir, A., Thermal Expansion Studies of Selected High-Temperature Thermoelectric Materials. *J. Electron. Mater.* **2009,** *38* (7), 1433-1442.
22. Perez, C. J.; Wood, M.; Ricci, F.; Yu, G.; Vo, T.; Bux, S. K.; Hautier, G.; Rignanese, G.-M.; Snyder, G. J.; Kauzlarich1, S. M., Discovery of multivalley Fermi surface responsible for the high thermoelectric performance in $Yb_{14}MnSb_{11}$ and $Yb_{14}MgSb_{11}$. *Sci. Adv.* **2021,** *7*, eabe9439.
23. Tan, W. J.; Liu, Y. T.; Zhu, M.; Zhu, T. J.; Zhao, X. B.; Tao, X. T.; Xia, S. Q., Structure, Magnetism, and Thermoelectric Properties of Magnesium-Containing Antimonide Zintl Phases $Sr_{14}MgSb_{11}$ and $Eu_{14}MgSb_{11}$. *Inorg. Chem.* **2017,** *56* (3), 1646-1654.
24. Tan, W.; Wu, Z.; Zhu, M.; Shen, J.; Zhu, T.; Zhao, X.; Huang, B.; Tao, X. T.; Xia, S. Q., $A_{14}MgBi_{11}$ (A = Ca, Sr, Eu): Magnesium Bismuth Based Zintl Phases as Potential Thermoelectric Materials. *Inorg. Chem.* **2017,** *56* (17), 10576-10583.
25. Sánchez-Portal, D.; Martin, R. M.; Kauzlarich, S. M.; Pickett, W. E., Bonding, moment formation, and magnetic interactions in $Ca_{14}MnBi_{11}$ and $Ba_{14}MnBi_{11}$. *Phys. Rev. B* **2002,** *65*, 144414.
26. Gallup, R. F.; Fong, C. Y.; Kauzlarich, S. M., Bonding Properties of $Ca_{14}GaAs_{11}$: A

Compound Containing Discrete $GaAs_4$ Tetrahedra and a Hypervalent As_3 Polyatomic Unit. *Inorg. Chem.* **1992,** *31* (1), 115-118.
27. Brown, S. R.; Kauzlarich, S. M.; Gascoin, F.; Snyder, G. J., $Yb_{14}MnSb_{11}$: New High Efficiency Thermoelectric Material for Power Generation. *Chem. Mater.* **2006,** *18* (7), 1873-1877.
28. Cox, C. A.; Toberer, E. S.; Levchenko, A. A.; Brown, S. R.; Snyder, G. J.; Navrotsky, A.; Kauzlarich, S. M., Structure, Heat Capacity, and High-Temperature Thermal Properties of $Yb_{14}Mn_{1-x}Al_xSb_{11}$. *Chem. Mater.* **2009,** *21* (7), 1354-1360.
29. Kunz Wille, E. L.; Jo, N. H.; Fettinger, J. C.; Canfield, P. C.; Kauzlarich, S. M., Single crystal growth and magnetic properties of the mixed valent Yb containing Zintl phase, $Yb_{14}MgSb_{11}$. *Chem Commun (Camb)* **2018,** *54* (92), 12946-12949.
30. Kunz Wille, E. L.; Grewal, N. S.; Bux, S. K.; Kauzlarich, S. M., Seebeck and Figure of Merit Enhancement by Rare Earth Doping in $Yb_{14-x}RE_xZnSb_{11}$ (x = 0.5). *Materials (Basel)* **2019,** *12* (5), 731-743.
31. Canfield, P. C.; Kong, T.; Kaluarachchi, U. S.; Jo, N. H., Use of frit-disc crucibles for routine and exploratory solution growth of single crystalline samples. *Philos. Mag.* **2016,** *96* (1), 84-92.
32. Smart-SAINT *APEX; Bruker AXS Inc*, 2007.
33. Smart; Bruker *SAINT: Area Detector Control and Integeration Software; Bruker AXS Inc*, Version 6.02 a; Bruker: Madison, Wisconsin, 2007.
34. Sheldrick, G. M., Crystal structure refinement with SHELXL. *Acta Crystallogr. C Struct. Chem.* **2015,** *71* (Pt 1), 3-8.
35. Cerretti, G.; Villalpando, O.; Fleurial, J. P.; Bux, S. K., Improving electronic properties and mechanical stability of $Yb_{14}MnSb_{11}$ via W compositing. *J. Appl. Phys.* **2019,** *126* (17), 175102.
36. Petříček, V.; Dušek, M.; Palatinus, L., Crystallographic Computing System JANA2006: General features. In *Zeitschrift für Kristallographie - Crystalline Materials*, 2014; Vol. 229, p 345.
37. Saiki, A.; Ishizawa, N.; Mizutani, N.; Kato, M., Structural change of C-rare earth sesquioxides Yb_2O_3 and Er_2O_3 as a function of temperature. *Yogyo Kyokai-Shi* **1985,** *93* (10), 649-654.
38. Borup, K. A.; Toberer, E. S.; Zoltan, L. D.; Nakatsukasa, G.; Errico, M.; Fleurial, J. P.; Iversen, B. B.; Snyder, G. J., Measurement of the electrical resistivity and Hall coefficient at high temperatures. *Rev. Sci. Instrum.* **2012,** *83* (12), 123902-123909.
39. Wood, C.; Zoltan, D.; Stapfer, G., Measurement of Seebeck Coefficient Using a Light-Pulse. *Rev. Sci. Instrum.* **1985,** *56* (5), 719-722.
40. Pillai, C. G. S.; Raj, P., Thermal conductivity of ThO_2 and $Th_{0.98}U_{0.02}O_2$. *J. Nucl. Mater.* **2000,** *277*, 116-119.
41. Kastbjerg, S.; Uvarov, C. A.; Kauzlarich, S. M.; Nishibori, E.; Spackman, M. A.; Iversen, B. B., Multi-temperature Synchrotron Powder X-ray Diffraction Study and Hirshfeld Surface Analysis of Chemical Bonding in the Thermoelectric Zintl Phase $Yb_{14}MnSb_{11}$. *Chem. Mater.* **2011,** *23* (16), 3723-3730.
42. Uvarov, C. A.; Ortega-Alvarez, F.; Kauzlarich, S. M., Enhanced high-temperature thermoelectric performance of $Yb_{14-x}Ca_xMnSb_{11}$. *Inorg. Chem.* **2012,** *51* (14), 7617-24.
43. He, A.; Wille, E. L. K.; Moreau, L. M.; Thomas, S. M.; Lawrence, J. M.; Bauer, E. D.; Booth, C. H.; Kauzlarich, S. M., Intermediate Yb valence in the Zintl phases $Yb_{14}MSb_{11}$(M =

Zn, Mn, Mg): XANES, magnetism, and heat capacity. *Physical Review Materials* **2020,** *4* (11) 114407.
44. Pomrehn, G. S.; Zevalkink, A.; Zeier, W. G.; van de Walle, A.; Snyder, G. J., Defect-controlled electronic properties in AZn_2Sb_2 Zintl phases. *Angew Chem. Int. Ed. Engl.* **2014,** *53* (13), 3422-6.
45. Zevalkink, A.; Smiadak, D. M.; Blackburn, J. L.; Ferguson, A. J.; Chabinyc, M. L.; Delaire, O.; Wang, J.; Kovnir, K.; Martin, J.; Schelhas, L. T.; Sparks, T. D.; Kang, S. D.; Dylla, M. T.; Snyder, G. J.; Ortiz, B. R.; Toberer, E. S., A practical field guide to thermoelectrics: Fundamentals, synthesis, and characterization. *Appl. Phys. Rev.* **2018,** *5* (2) 021303.
46. Goldsmid, H. J.; Sharp, J. W., Estimation of the thermal band gap of a semiconductor from Seebeck measurements. *J. Electron. Mater.* **1999,** *28* (7), 869-872.
47. Askeland, D. R.; Fulay, P. P.; Wright, W. J., *The Science and Engineering of Materials, SI Edition*. CL-Engineering: 2011.
48. Hu, Y. F.; Bux, S. K.; Grebenkemper, J. H.; Kauzlarich, S. M., The effect of light rare earth element substitution in $Yb_{14}MnSb_{11}$ on thermoelectric properties. *Journal of Materials Chemistry C* **2015,** *3* (40), 10566-10573.
49. Toberer, E. S.; Cox, C. A.; Brown, S. R.; Ikeda, T.; May, A. F.; Kauzlarich, S. M.; Snyder, G. J., Traversing the Metal-Insulator Transition in a Zintl Phase: Rational Enhancement of Thermoelectric Efficiency in $Yb_{14}Mn_{1-x}Al_xSb_{11}$. *Adv. Funct. Mater.* **2008,** *18* (18), 2795-2800.
50. Borup, K. A.; de Boor, J.; Wang, H.; Drymiotis, F.; Gascoin, F.; Shi, X.; Chen, L. D.; Fedorov, M. I.; Muller, E.; Iversena, B. B.; Snyder, G. J., Measuring thermoelectric transport properties of materials. *Energy Environ. Sci.* **2015,** *8* (2), 423-435.
51. Snyder, G. J., Application of the compatibility factor to the design of segmented and cascaded thermoelectric generators. *Appl. Phys. Lett.* **2004,** *84* (13), 2436-2438.

For table of contents use only:

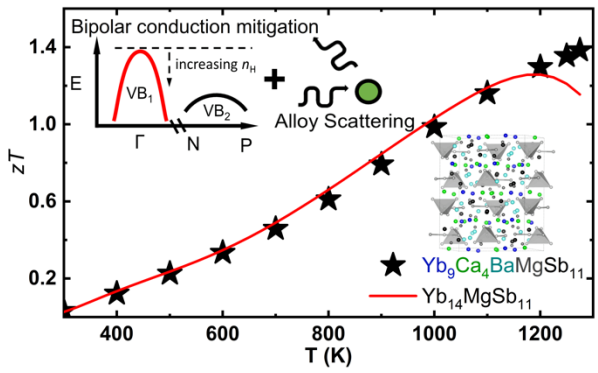

The series $Yb_{13-x}Ca_xBaMgSb_{11}$ (x = 1 – 6) has been synthesized and structure and transport properties measured. The evolution of properties can be understood employing the electronic structures of $A_{14}MgSb_{11}$ (A = Yb, Ca). The samples show a sustained Seebeck coefficient at high temperatures (> 1000 K) and thermal conductivity is reduced by alloy scattering leading to a $zT_{1200\ K} \sim 1.3$.